CAMBRIDGE
UNIVERSITY PRESS

Article

Neocrystallization of clay minerals in the Alhama de Murcia Fault (southeast Spain): implications for fault mechanics

Isabel Abad[1]*, Juan Jiménez-Millán[1], Catalina Sánchez-Roa[2], Fernando Nieto[3] and Nicolás Velilla[4]

[1]Departamento de Geología and CEACTierra, Unidad Asociada IACT (CSIC-UGR), Universidad de Jaén, Campus Las Lagunillas s/n, 23071 Jaén, Spain; [2]Department of Earth Sciences, University College London, London, UK; [3]Departamento de Mineralogía y Petrología and IACT (CSIC-UGR), Facultad de Ciencias, Universidad de Granada, Avda. Fuentenueva s/n, 18002 Granada, Spain and [4]Departamento de Mineralogía y Petrología, Facultad de Ciencias, Universidad de Granada, Avda. Fuentenueva s/n, 18002 Granada, Spain

Abstract

Two preferred textures were observed in the Alhama de Murcia Fault rocks: (a) foliated bands (>100 μm thick) rich in well-crystallized dioctahedral micas, quartz, hematite and dolomite; and (b) ultrafine-grained bands (<100 μm thick) made of patches composed of small mica crystals (<15 μm) and dispersed Fe-oxides. In both textures, kaolinite forms intergrowths or patches of randomly oriented crystals filling gaps or opening layers of presumably inherited detrital mica crystals, which is interpreted as an epitaxial growth from fluids. The Na/K ratio of mica crystals in the thin ultrafine-grained bands shows a wider range than the micas from the foliated bands including muscovitic, intermediate Na/K and paragonitic compositions. The absence of the 0.98 nm intermediate peak in the diffractograms indicates that the small micas are submicroscopically paragonite and phengite intergrowths. The d_{001} values of the K-dioctahedral micas in the <2 μm and whole fractions are clearly different from each other. The d_{001} values of micas of the <2 μm fraction are larger, indicating a higher K and lower Na content in the small micas. Their composition corresponds to lower temperatures, suggesting their growth during a genetic episode in the fault. The textural relationships indicate a late growth of kaolinite, probably due to the fluid–rock interaction along fault planes and fractures. The neoformed clay minerals might alter the stability of the fault plane. The absence of expandable clay minerals and the relatively high frictional strength of kaolinite under wet conditions might explain the observed velocity-neutral behaviour of this gouge and earthquake propagation towards the surface.

Keywords: Alpujárride, electron microscopy, EPMA, friction, kaolinite, mica

The collision of the Eurasian and the African plates renders the southern Iberian Peninsula a tectonically active area. Many active faults have been recognized, including the Alhama de Murcia, Baza, Carboneras and Palomares faults, some of which have recently been responsible for large-magnitude earthquakes, such as the 5.1 magnitude Lorca earthquake in May 2011. This earthquake caused significant damage in the Murcia region, a total of nine deaths and an estimated 400 injuries.

The internal structure of these major strike slip fault zones has been studied thoroughly in the past (Alhama de Murcia: Masana *et al.*, 2004; Baza: Alfaro *et al.*, 2008; Carboneras: Faulkner *et al.*, 2003; Rutter *et al.*, 2012; Palomares: Booth-Rea *et al.*, 2004; among others), but less attention has been given to mineralogical and microstructural characterization and to the physical processes related to the accommodation of the deformation in the mineral phases in fault rocks (*e.g.* for Carboneras and Palomares faults, see Jiménez-Millán *et al.*, 2015; Abad *et al.*, 2017).

The role of phyllosilicates within active fault systems and in relation to earthquake dynamics is a field of ongoing research. The brittle deformation of rocks in active fault systems increases the interaction between low-temperature fluids and rocks and frequently causes an enrichment of clay minerals (illite, chlorite, smectite and interstratifications of these clays) (Evans & Chester, 1995; Solum *et al.*, 2003; Torgersen & Viola, 2014). Understanding the genetic relations affecting clays in low-temperature geological environments is complicated by the absence of chemical equilibrium, the small grain size (which makes textural studies difficult) and the identification of common intergrowths of phases. Some of the key factors controlling active deformation processes in large fault zones are: (1) the clay mineral assemblages; (2) the chemical composition and swelling behaviour of clay minerals; and (3) the influence of clay minerals on fluid circulation properties (*e.g.* Sibson, 1986; Vrolijk & van der Pluijm, 1999). In addition, the occurrence of clay-rich fault rocks has been suggested as contributing to the weakening of faults (Wang, 1984; Imber, 2001; Lockner *et al.*, 2011) and is possibly a controlling factor in governing seismic stick-slip *vs.* creep mechanisms (Faulkner *et al.*, 2003; Schleicher *et al.*, 2010; Torgersen & Viola, 2014) due to their low friction coefficients,

*E-mail: miabad@ujaen.es

Cite this article: Abad I, Jiménez-Millán J, Sánchez-Roa C, Nieto F, Velilla N (2019). Neocrystallization of clay minerals in the Alhama de Murcia Fault (southeast Spain): implications for fault mechanics. *Clay Minerals* **54**, 1–13. https://doi.org/10.1180/clm.2019.2

continuous layers of water on their main cleavage planes and velocity-dependent behaviour (mechanical stability under friction) (Lockner et al., 2011; Schleicher et al., 2013).

In this study, X-ray diffraction (XRD), scanning electron microscopy (SEM), transmission electron microscopy (TEM) and the electron microprobe have been used to characterize the fault-rock mineralogy of the most seismic segment of the Alhama de Murcia Fault (AMF), placing special emphasis on the clay mineralogy. This petrographic characterization of fault rocks aimed to determine the potential neoformation of clay minerals during faulting and to evaluate the possible influence of the mineralogy, especially the phyllosilicates, on the seismic activity and frictional properties of this fault (Niemeijer & Vissers, 2014).

Geological setting and materials

The Betic Cordillera (southern Spain) is the westernmost European Alpine chain. This ENE–WSW-trending fold-and-thrust belt is composed of the External Zone and the Internal Zone, or Alboran domain (Fig. 1a). The External Zone is characterized by Mesozoic to Tertiary rocks corresponding to the Iberian Plate palaeomargin, situated on top of the Variscan basement. The Internal Zone consists of a thrust stack of metamorphic complexes affected by major tectonism and large displacements during the early Miocene (Sanz de Galdeano, 1990). Superimposed on these structures are Neogene to Quaternary sediments filling the intramontane basins, limited by E–W and NE–SW faults (Montenat & Ott D'Estevou, 1995). Moreover, Middle Miocene to Pleistocene calc-alkaline to K-rich volcanic rocks crop out in the Cabo de Gata area (Duggen et al., 2004).

The Neogene and Quaternary faulting activity in the southeastern Iberian Margin (Trans-Alboran Shear Zone) is dominated by a large NE–SW left-lateral strike-slip fault system, which is responsible for the intense deformation of the alpine crystalline protoliths. The biggest sinistral strike-slip faults are the Carboneras Fault (Bell et al., 1997), the Palomares Fault (Booth-Rea et al., 2004) and the AMF (Martínez-Díaz et al., 2012a, 2012b) (Fig. 1). This system is by far the longest continuous fault system mapped in the Betic Cordillera and therefore would be expected to generate large-magnitude earthquakes (Gracia et al., 2006). However, seismicity in the area is mainly characterized by low- to moderate-magnitude events. Nevertheless, occasional large, destructive earthquakes have occurred in the region, therefore comprising significant earthquake and tsunami hazards to the coasts of Spain and North Africa (IGN, 2001; Masana et al., 2004).

The AMF trends NE–SW with a 55°–65° NW dip and extends for 100 km from the Huercal-Overa depression to the outskirts of Murcia (Fig. 1). The history of the AMF reflects the tectonic inversion from an extensional to a strike-slip tectonic setting that occurred in the eastern Betics (Ferrater et al., 2015). The tectonic inversion prompted large Pliocene to Quaternary strike-slip faults to reactivate previous Late Miocene normal faults associated with NW–SE and NE–SW extension (Meijninger & Vissers, 2006) within a diffuse plate boundary where African and Eurasian plates currently converge at a rate between 4 and 5 mm/year (Alfaro et al., 2012). From the Late Miocene to the present, the faulted basement has been folded and uplifted (Alfaro et al., 2012) and strike-slip tectonics dominate, especially along the NE–SW faults. According to Meijninger & Vissers (2006), the AMF initiated its activity during the Late Miocene, thus producing an 'intra-Tortonian unconformity'; the presence of tilted sediments underlying this unconformity cut by extensional normal faults suggests that the AMF should have started its activity after the Tortonian. The oldest alluvial fans related to the AMF were deposited during the Pleistocene, indicating that strike-slip activity and folding associated with the AMF was probably initiated during the Pliocene or Quaternary (Meijninger & Vissers, 2006).

According to Martínez-Díaz et al. (2012a), the AMF is subdivided into four segments: (1) Goñar–Lorca (37 km), with moderate concentration of epicentres and the evident relief of the Las Estancias range; (2) Lorca–Totana (16 km), where the fault controlled the evolution of the Neogene Lorca basin, where Quaternary sediments are trapped by the recent activity of the fault and with the maximum concentration of seismicity; (3) Totana–Alhama de Murcia (17 km); and (4) Alhama de Murcia–Alcantarilla (23 km), which controlled the evolution of a depression to the NW, but shows little geomorphological fault expression.

Twenty-seven samples were collected from the Lorca–Totana segment (Fig. 1b, Table 1), which is a 16 km-long structure composed of two main NE–SW fault branches: (1) a northwestern steeply dipping reverse fault (70° NW) bounding the La Tercia range to the SE; and (2) a southeastern left-lateral and high-angle reverse fault dipping to the SE with oblique slip. The studied samples belong to the first fault branch, where the fault deforms the Alpujárride Complex, one of the thrust stacks of the metamorphic complexes within the Betic Internal Zone. The samples were taken directly from the fault plane of the AMF, including a trench uncovered after the 2011 earthquake (Fig. 2). During the collection, the outer 10–20 cm of material was removed to avoid any contamination of samples by surface weathering.

Methodology

X-ray diffraction data were obtained from random powders and oriented aggregates (whole-rock samples and <2 μm fractions) after washing with distilled water to remove salts. Oriented aggregates were prepared by sedimentation on glass slides and the <2 μm fraction was separated by centrifugation. Ethylene glycol (EG) solvation allowed the identification of expandable minerals (smectite, interstratified layers, etc.).

X-ray diffractograms were obtained with a PANalytical X'Pert Pro diffractometer (Cu-$K\alpha$ radiation, 45 kV, 40 mA) equipped with an X'Celerator solid-state linear detector, using a step increment of 0.008°2θ and a counting time of 10 s/step (Department of Mineralogy and Petrology, University of Granada). Scans between 3° and 62°2θ were performed for the dry samples, while for the EG-solvated samples scans were performed between 2° and 30° 2θ to identify expandable minerals. The basal spacing of micas (d_{001}) was determined precisely from the (00,10) reflection using the quartz of the sample as the internal standard.

Carbon-coated, polished, thin sections were examined by SEM using back-scattered electron (BSE) imaging in atomic number contrast mode and energy-dispersive X-ray (EDX) analysis to obtain textural and chemical data. These observations were carried out with a Merlin Carl Zeiss scanning electron microscope at the Centro de Instrumentación Científico-Técnica, CICT (University of Jaén) and a Leo 1430-VPSEM at the Centro de Instrumentación Científica, CIC (University of Granada). An accelerating voltage of 20 kV with a beam current of 1–2 nA and counting time of 50 s were used to analyse the silicates by SEM using the following standards: albite (Na), periclase (Mg), wollastonite (Si and Ca) and orthoclase (K) and synthetic Al_2O_3
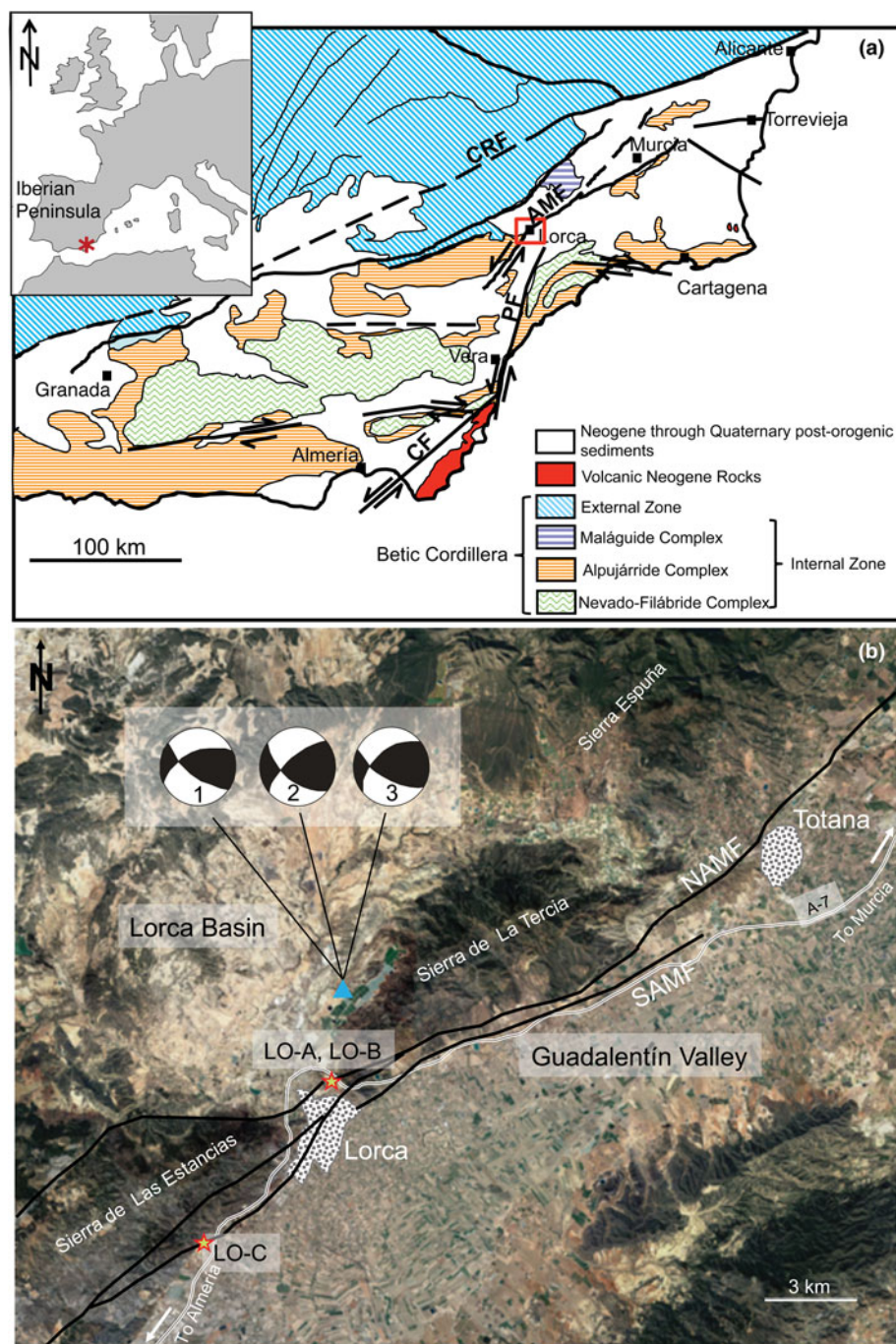
Fig. 1. (a) Geological map of the Trans-Alborán Shear Zone with the main Neogene faults (SE Spain) and the location of the study area. AMF = Alhama de Murcia Fault; CF = Carboneras Fault; CRF = Crevillente Fault; PF = Palomares Fault. Modified from Gracia *et al.* (2006). (b) Location map with the projection of the Alhama de Murcia Fault (NAMF and SAMF, Northern and Southern branches of the fault, respectively) including the sampling points (LO-A, LO-B and LO-C). The triangle is the mainshock of the Lorca 2011 seismic sequence taken from López-Comino *et al.* (2012). Focal solutions of the mainshock from several agencies are shown (1 = Instituto Andaluz de Geofísica; 2 = Instituto Geográfico Nacional; 3 = Harvard University).

(Al), Fe_2O_3 (Fe) and $MnTiO_3$ (Ti and Mn). Analytical data were ZAF (atomic number, absorption and fluorescence) corrected. Electron probe microanalysis (EPMA) of micas corresponding to different textural zones was performed by wavelength-dispersive spectroscopy (WDX) on a Cameca SX100 at the CIC (University of Granada). The instrument was set at an accelerating voltage of 15 kV, with a beam current of 15 nA and an electron beam diameter of <5 μm. Data were reduced using the procedure of Pouchou & Pichoir (1985) and the standards used were albite, sanidine, periclase, diopside, quartz, vanadinite, rutile, fluorite and synthetic oxides (Al_2O_3, Fe_2O_3, NiO and $MnTiO_3$).

3 mm copper rings with a 1 mm-diameter hole were glued with an epoxy resin to the areas selected for further study by high-resolution TEM (HRTEM). After drying for 24 h, the rings were removed by heating the thin section. The rings were cleaned and ion-thinned to a suitable thickness for TEM study in a Fischione-1010 ion mill (CICT, University of Jaén). The initial conditions for the ion thinning were 12°, 5 kV and 5 mA until the first hole opened; from there, they underwent an intermediate stage with 8°, 4 kV and 5 mA, followed by a final stage with 5°, 3 kV and 5 mA.

The HRTEM data were obtained using a Philips CM20 scanning transmission electron microscope (STEM), operated at 200 kV and with a point-to-point resolution of 0.27 nm in TEM mode and 5 nm in STEM mode at the CIC (University of Granada).

Table 1. Sample list of the studied rocks with the geographic coordinates and bulk mineralogy determined by XRD and SEM.

Samples	Geographic coordinates	Mineral composition (Qz, Ilt/Ms, Pg and Kln in all the samples)
LO-A-01	37° 41′ 21.24″ N/1° 41′ 0.79″ W	Chl, Cal
LO-A-02		Chl, Cal
LO-A-03		Chl, Sme, Cal
LO-A-04		Chl, Sme, Cal, Hem
LO-A-05		Dol
LO-A-06		
LO-A-07		
LO-A-08	37° 41′ 19.59″ N/1° 41′ 05.93″ W	Kfs
LO-A-09		Chl, Cal
LO-A-10		Cal
LO-A-11		Cal, Dol, Hem
LO-A-12	37° 41′ 20.22″ N/1° 41′ 08.97″ W	Cal
LO-A-13		Dol, Hem
LO-A-14		Dol, Hem
LO-A-15		Hem, Kfs
LO-A-16		Chl, Dol, Gp
LO-A-17		Chl, Dol, Gp
LO-A-18		Chl, Dol, Gp
LO-A-19		Chl, Cal, Dol, Hem
LO-B-01	37° 41′ 20.31″ N/1° 41′ 20.89″ W	Dol
LO-B-02		Chl, Hem
LO-C-01	37° 38′ 16.79″ N/1° 44′ 47.39″ W	
LO-C-02		Dol, Hem, Mws
LO-C-03		Hem
LO-C-04		Hem
LO-C-05		Hem
LO-C-06		Hem

Abbreviations of mineral names after Whitney and Evans (2010).
In italics are samples studied by SEM; in bold are samples studied by HRTEM.

Results

The bulk-rock samples and oriented clay fractions contain abundant K- and Na-dioctahedral micas and minor quartz. Carbonates (calcite and/or dolomite), gypsum, chlorite and hematite are present only in some samples (Fig. 3). There were no significant changes after EG solvation, indicating the absence of expandable phases such as smectite, except for minimal amounts in two samples. Kaolinite is present in all samples (Table 1).

Polished thin sections from the fault rocks show that they are composed of very fine-grained and well-developed gouge material (Fig. 4).

Specifically, rocks from the fault core are made of:

a) Foliated bands (>100 μm thick) that are rich in well-crystallized muscovite, paragonite and quartz, including dolomite and hematite crystals frequently >20 μm in size (Fig. 5a). In some cases, dolomite grains exhibit intact cores and rims with localized disaggregation, holes and Fe-oxide crystallization (Fig. 5b).

b) Thin, ultrafine-grained bands (<100 μm thick) characterized by the presence of numerous holes and vesicles (Fig. 5c). These domains are made of patches of small crystals (<15 μm) with mica bulk composition. These patches host dispersed crystals of Fe-oxide and a network of dolomite skeletal crystals (Fig. 5d,e).

c) Patches of kaolinite made of randomly oriented crystals ranging in size from 30 μm to <2 μm and usually filling gaps in the rock structure (Fig. 5b). Kaolinite are also observed in foliated bands associated with K- and Na-micas, with the same orientation and sometimes intergrown in stacks (Fig. 5e,f).

At TEM scale, the mineralogical characterization of the samples confirms the data obtained by XRD and SEM. Some areas contain large and well-crystallized packets of dioctahedral micas (several hundreds of nanometres in size) with a 2*M* polytype (Fig. 6a), probably related to the thick foliated bands described by SEM. There are also smaller mica grains (<100 nm) with strain contrast orthogonal or oblique to the lattice fringes, probably generated by tectonic stress (Fig. 6b,c). Kaolinite packets forming aggregates of parallel and subparallel grains were identified inside voids (Fig. 7a). In addition, electron diffraction images showed that, in some areas, paragonite, muscovite and kaolinite form parallel or low-angle intergrowths at the nanoscale (Fig. 7b). These intergrowths are not very obvious in the lattice fringe images due to the fast beam damage of the kaolinite packets. Fe-oxide aggregates, formed by randomly oriented and prismatic grains, were also identified at the nanometre scale (Fig. 8).

Chemical analyses obtained by SEM-EDX and EPMA give similar results (Fig. 9, Tables 2, 3). Both K- and Na-dioctahedral micas are present. K-dioctahedral micas corresponding to the foliated bands with well-crystallized grains are characterized by compositions typical of muscovites or phengites rather than illites. The phengitic component is the main component responsible for the negative correlation between Al and Fe + Mg octahedral atoms (Fig. 9a). The sum of interlayer cations is, in most cases, higher
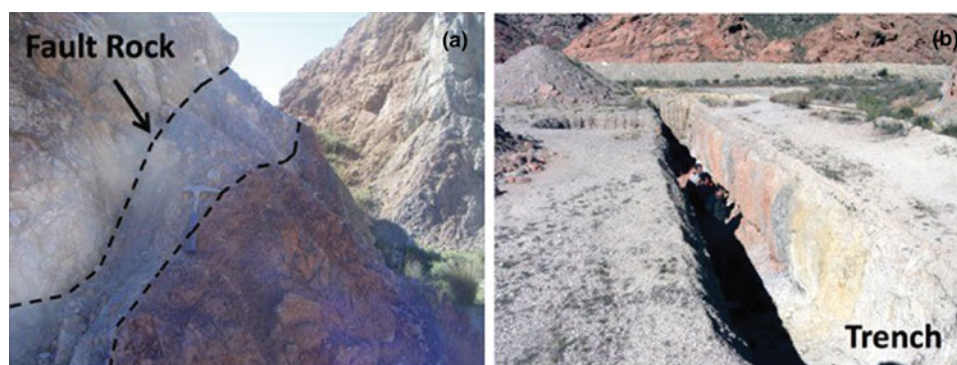

Fig. 2. View of the outcrops. (a) Detail of fault rocks. (b) Trench where samples LOA16–19 were collected.
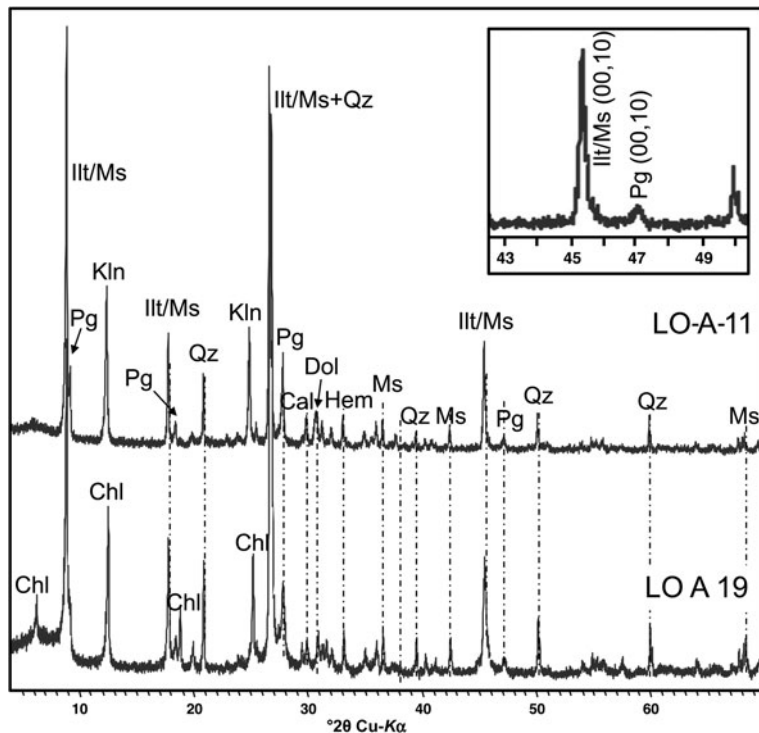
Fig. 3. Representative X-ray diffractograms corresponding to samples from Alhama de Murcia Fault rocks. Inset: Enlarged (00,10) mica peak region, showing the presence of only two peaks corresponding to muscovite (phengite) and paragonite. Cal = calcite; Dol = dolomite; Chl = chlorite; Hem = hematite; Ilt = illite; Kln = kaolinite; Ms = muscovite; Pg = paragonite; Qz = quartz.

than 0.85 atoms per formula unit (apfu) (Fig. 9b), and some of the analysed K-micas have significant Na content (up to 0.30 apfu) (Fig. 9c,d). The mica crystals analysed in the thin, ultrafine-grained bands also have a sum of interlayer cations that is very similar to the well-crystallized grains of the foliated bands (Fig. 9b). Nevertheless, the Na/K ratio shows a rather wider range than that of the micas from the foliated bands (Fig. 9c,d), covering all of the field of intermediate compositions between K and Na. They show in general a larger variation in chemical composition, whereas the well-crystallized grains from the foliated bands show much less difference. Muscovitic, phengitic, intermediate Na/K and paragonitic compositions have been identified in the ultrafine-grained bands with predominance of the intermediate Na/K-micas (Fig. 9, Tables 2, 3). In addition, in Fig. 9, chemical data corresponding to the 2M K-dioctahedral micas from the Alpujárride protolith in the area of Sierra Espuña (Abad et al., 2003) have been included for comparison.

The trioctahedral chlorites, which have an Fe/(Fe + Mg) ratio of ~0.60, correspond mainly to the chamosite (Fe-rich) variety (Table 4). The octahedral sums are near 6, which precludes the application of chlorite geothermometry, as such values render the margin of error of the method unacceptable; however, together with the low Si content, they are characteristic of high-temperature chlorites (Bourdelle & Cathelineau, 2015; Vidal et al., 2016). Kaolinite analyses fit the theoretical formula of a pure, Al-rich composition (Table 4).

Discussion

Neoformation of clay minerals in the AMF

The compositional differences between the well-crystallized packets of dioctahedral micas (mostly muscovites, with some phengitic component) and the mica crystals analysed in the thin, ultrafine-
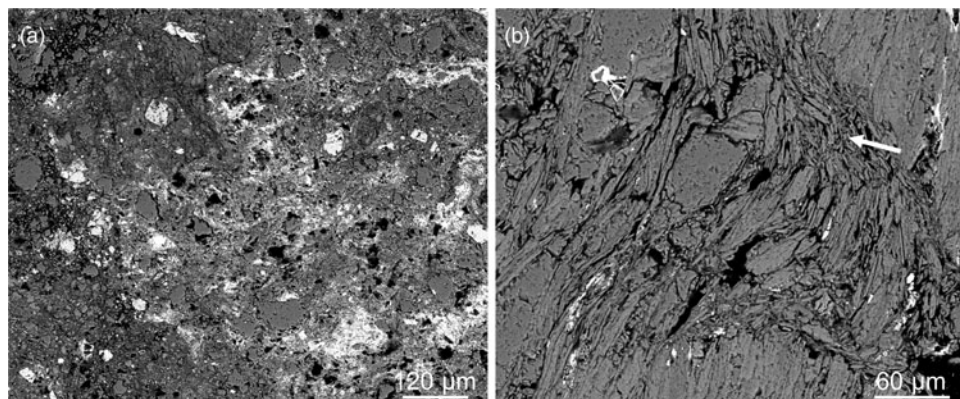

Fig. 4. BSE images showing the textural aspect of the fault rocks. (a) Fine-grained material corresponding to the gouge with poorly sorted quartz grains with irregular shapes and Fe-oxides. (b) Phyllosilicates stacks with curved shapes and signs of grain-size reduction (arrow).
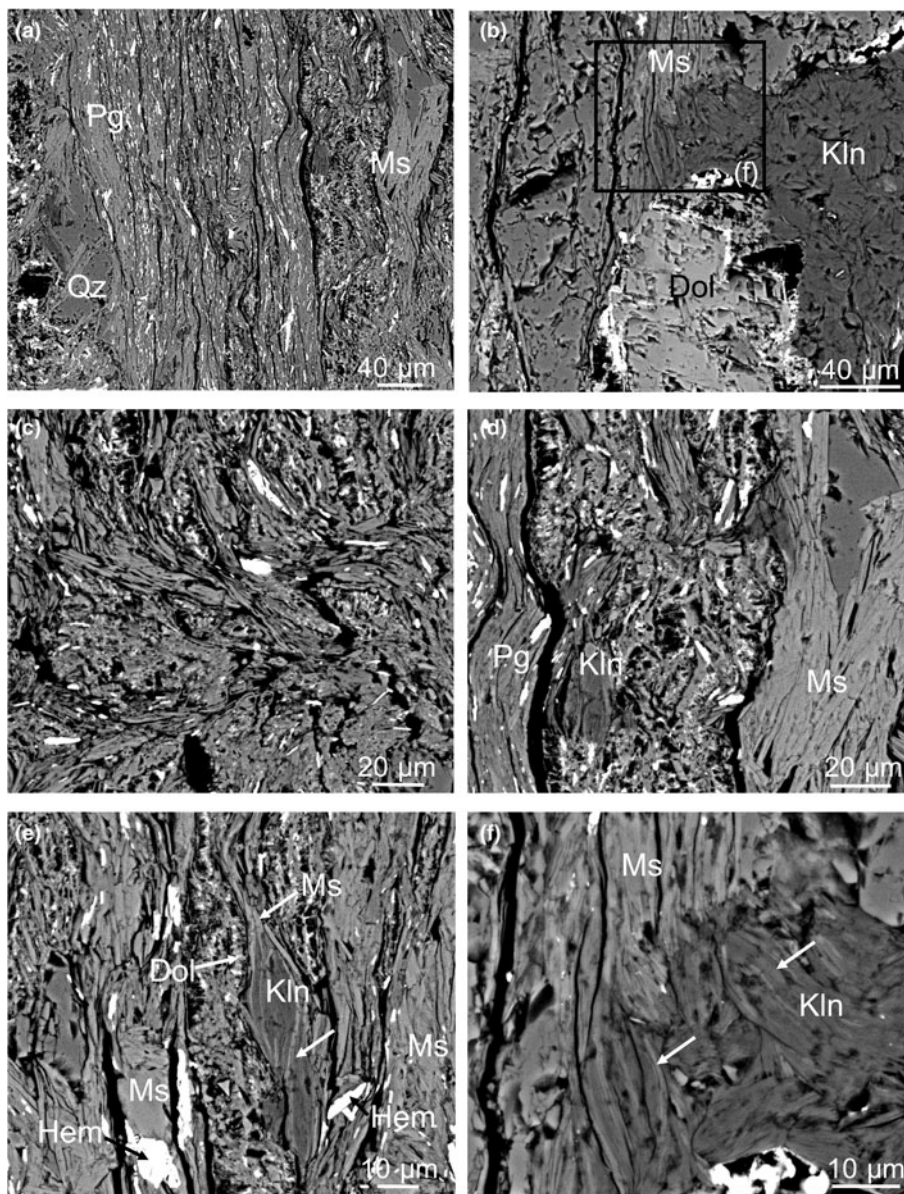
Fig. 5. BSE images of the fault rocks. (a) An example of a foliated band composed of micas, quartz and Fe-oxides. (b) Dolomite grain showing rims with localized disaggregation and Fe-oxide crystallization, partially surrounded by a patch of kaolinite. (c) Poorly crystalline material characterized by the presence of numerous holes alternating with thin and very-fine-grained phyllosilicate bands. (d) Detail of the network of dolomite skeletal crystals between two foliated bands. (e) Another example of the network between phyllosilicate bands, one of them with a stack of kaolinite with some K-mica packets intergrown (white arrows). (f) Detail of the patch of kaolinite from (b), in which mica packets intergrown with kaolinite (white arrows) are distinguished. Dol = dolomite; Hem = hematite; Kln = kaolinite; Ms = K-rich dioctahedral mica; Pg = Na-rich dioctahedral mica; Qz = quartz.

grained bands with predominance of intermediate compositions between muscovite and paragonite (Figs 9, 10) suggest they have different origins. The compositions determined by EPMA for the micas of the thin, ultrafine-grained bands are well within the compositional gap between muscovite and paragonite (Guidotti *et al.*, 1994; Coggon & Holland, 2002; Parra *et al.*, 2002). They might correspond to the so-called interstratified paragonite/muscovite (Frey, 1969, 1978) or metastable intermediate Na/K-mica (Jiang & Peacor, 1993), later interpreted by Livi *et al.* (2008) as white mica nanodomains. Nevertheless, such a mineral entity is characterized in all of the described cases (cited references in the two previous sentences) by an intermediate peak at 0.98 nm, which in the AMF samples is completely absent. The areas of the diagrams corresponding to the (00,10) peaks of micas show two well-differentiated peaks, corresponding to muscovite (or phengite) and paragonite, respectively (Fig. 3, inset). Therefore, the small mica crystals shown in the thin, ultrafine-grained bands (Fig. 10a) are interpreted only

submicroscopically as paragonite and phengite intergrowths under the resolution of compositional maps (Fig. 10b,c,d) and microanalyses of EPMA (Fig. 9), as is frequently described in the literature (*e.g.* Shau *et al.*, 1991; Livi *et al.*, 2008 and references therein). In conclusion, most compositions of the thin, ultrafine-grained bands determined by EPMA and SEM do not correspond to individual mica grains, but rather represent mixed compositions of a fine intergrowth between Na- and K-micas under the resolution of EPMA and SEM analyses (∼2 μm).

To compare the real Na/K content of the micas in the thin, ultrafine-grained bands with that of the foliated bands, an indirect approach was used that was free of the effects of their mutual contamination. As K has a significantly larger atomic radius than Na, the d_{001} of micas is deeply influenced by the Na/K ratio (Guidotti *et al.*, 1992). The lattice parameters depend on the average compositions of the minerals at the lattice level; hence, they are free of the effects of mutual contamination by the two micas. The measurement of the d_{001} parameter of the K-dioctahedral micas in
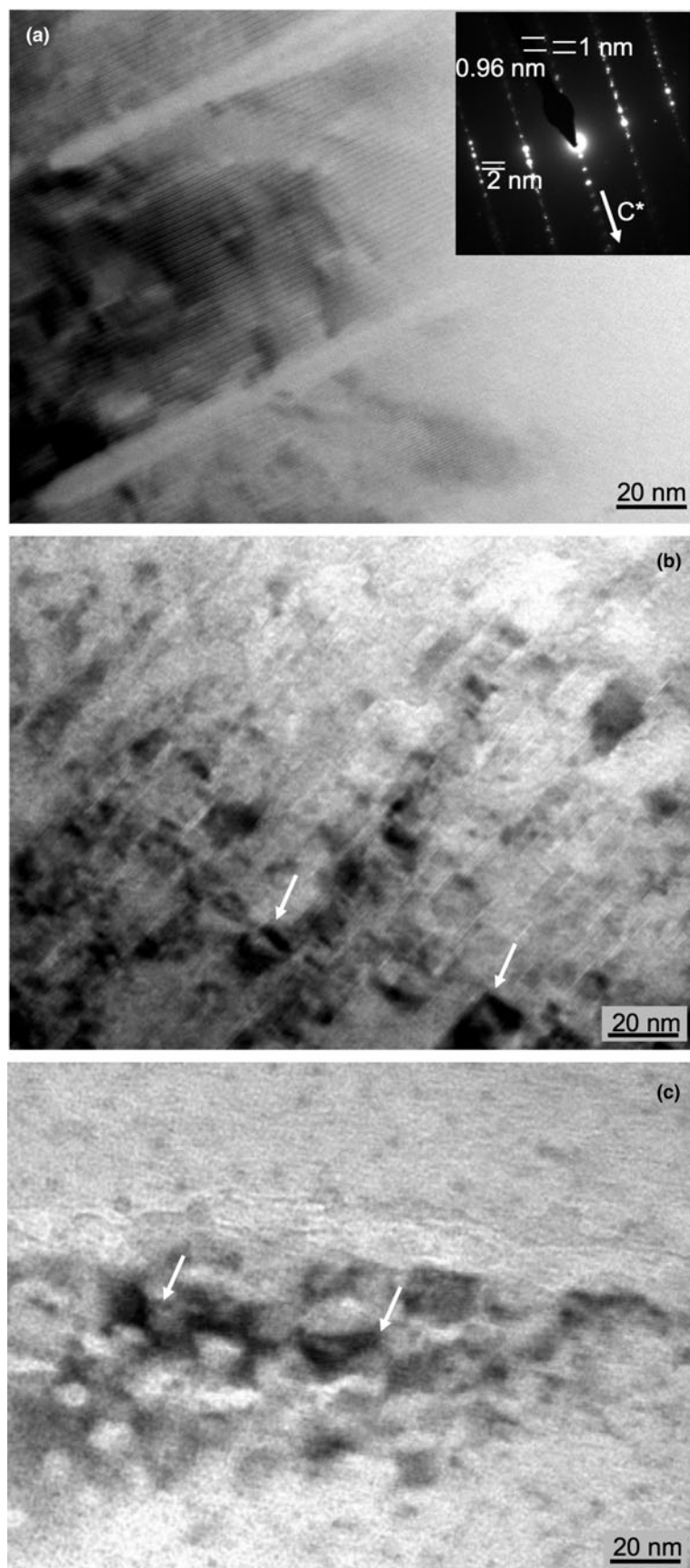
Fig. 6. (a) TEM lattice fringe image with large dioctahedral mica crystals showing a 2 nm periodicity; the electron diffraction pattern shows the presence of basal spacings corresponding to paragonite (0.96 nm) and muscovite (1 nm). (b, c) TEM lattice fringe images corresponding to thin dioctahedral mica packets with a very damaged appearance (see arrows).
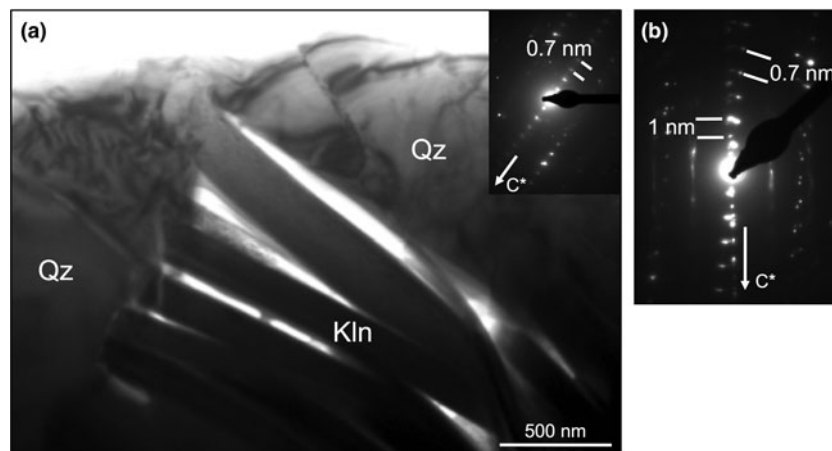
Fig. 7. (a) Low-magnification image of a kaolinite aggregate surrounded by quartz grains. (b) Selected area electron diffraction showing the parallel and subparallel relations between dioctahedral micas and kaolinite. Kln = kaolinite; Qz = quartz.

oriented aggregates of the <2 μm and whole fractions allows us to consider whether the former include predominantly the small micas of the thin, ultrafine-grained bands, while the latter include the two kinds of micas (foliated and ultrafine-grained bands). A clear difference between the two populations is observed (Fig. 11), with the d_{001} of micas of the <2 μm fraction being greater, which indicates a higher K and lower Na content (Guidotti *et al.*, 1992) of the small micas in the thin, ultrafine-grained bands. As the two end members of the muscovite-paragonite solvus are present (Fig. 3), more extreme compositions, which have a higher K content in muscovite limb of the solvus, represent a lower temperature of formation (Guidotti *et al.*, 1994; Coggon & Holland, 2002; Parra *et al.*, 2002). This lower temperature is probably responsible for the very small grain size of the components of the intergrowth between K- and Na-micas. It is concluded that the micas of the thin, ultrafine-grained bands have a different composition from those of the foliated bands, and this composition corresponds to a lower temperature of formation. Therefore, the micas in the thin, ultrafine-grained bands do not simply result from the breaking and reorientation of the larger metamorphic mica crystals of the original rocks, but rather they have grown during a genetic episode in the fault. The reasonably wide range of values of phengitic content of micas inherited from the protolith at the sample level is a common characteristic of the Alpujárride rocks

and is a consequence of the isothermal decompression path followed by the Alpujárride Complex from at least 10 kbar (Azañón & Crespo-Blanc, 2000).

Chlorite is the other common phyllosilicate in the Alpujárride rocks. In the fault samples, all of the analysed chlorites show low Si content and octahedral sums near 6 (Table 4), indicating high amesite and low sudoite components, respectively, which, in turn, indicate a high temperature of formation of the chlorites, but preclude an exact determination of the temperature (Bourdelle & Cathelineau, 2015; Vidal *et al.*, 2016). Therefore, similarly to the micas of the foliated bands, chlorites in the fault rocks have chemical characteristics that are similar to their counterparts of the protolith (Abad *et al.*, 2003), suggesting a metamorphic origin.

In fact, the protolith of the studied rocks is a grey phyllite that is widely distributed in all of the Alpujarride Complex, which may be described from the nearest outcrops in the southern part of Sierra Espuña (Fig. 1b). These rocks are composed of K- and Na-dioctahedral micas, chlorite, quartz, hematite, carbonates (calcite and dolomite) and retrograde smectite (Nieto *et al.*, 1994). The large amounts of K- and Na-micas in the fault rocks are consistent with the mineralogy of the protolith, which was characterized in detail by Abad *et al.* (2003). Nevertheless, the textural differences between the Alpujárride protolith and the fault rocks are remarkable: a well-developed foliation in the phyllites, affecting even quartz, oxide and carbonate grains (*e.g.* see fig. 3 in Abad *et al.*, 2003), compared with the very-fine-grained breccias in the fault rocks (Figs 4, 5). In addition, to our knowledge, kaolinite has not been described in the protolith, which is at odds with its ubiquitous presence in all of the samples collected in or near the fault plane (Table 1).

The presence of authigenic kaolinite should be related to the fluid–rock interaction along fault planes and fractures. In some cases, kaolinite is finely intergrown with small mica crystals (Figs 5e,f, 7b). Figure 5e shows how the newly formed kaolinite opens the layers of presumably inherited detrital mica crystals. This has been interpreted traditionally as an epitaxial growth from fluids, in which the mica layers act as templates facilitating kaolinite growth (*cf.* Arostegui *et al.*, 2001 and references therein). In other cases, kaolinite forms patches of randomly oriented crystals filling gaps in the rock structure. We have not found any proof of transformation of previous mica by kaolinite by means of a topotaxial mechanism. Overall, the textural relationships between mica and kaolinite indicate that the latter grew after
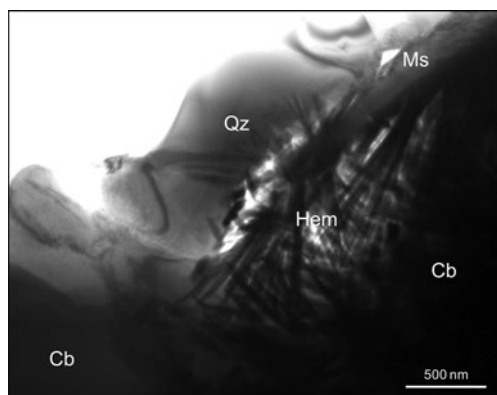

Fig. 8. Low-magnification image of an Fe-oxide aggregate at nanoscale. Cb = carbonates (calcite and dolomite); Hem = hematite; Ms = K-rich dioctahedral mica; Qz = quartz.
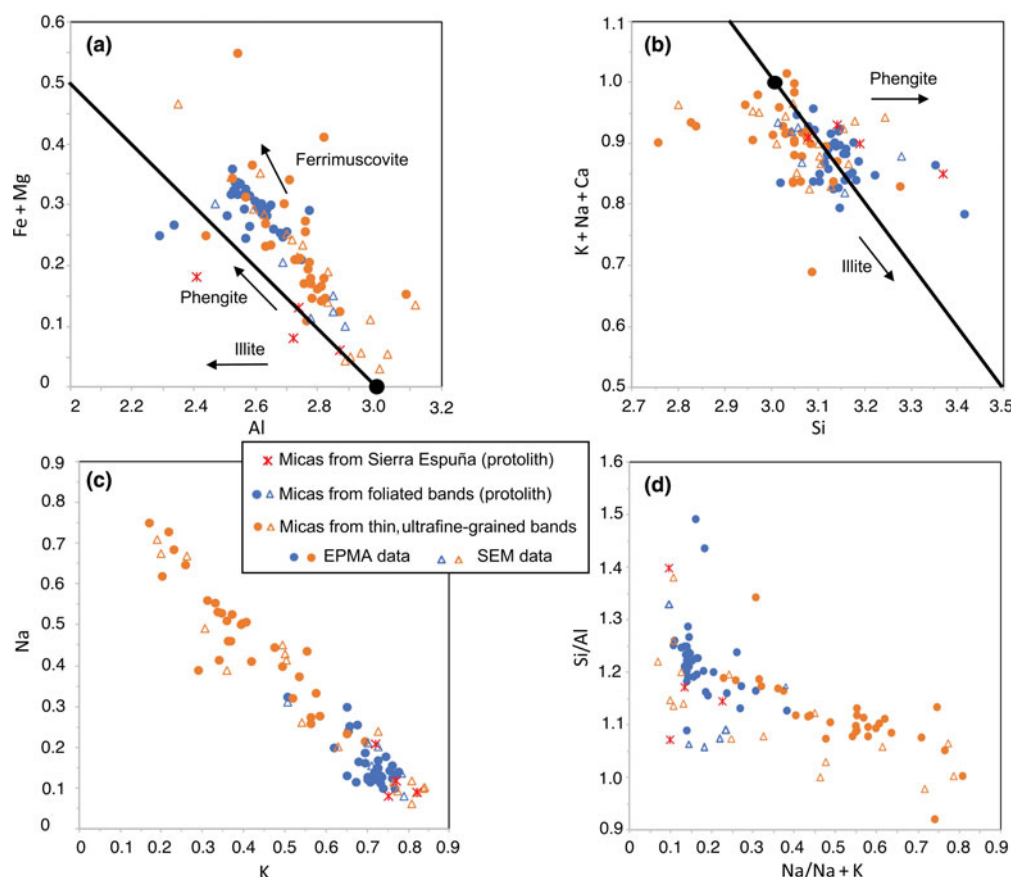
Fig. 9. Relationships among the chemical components of the dioctahedral micas studied by SEM/EDX and EPMA/WDX. (a) Al *vs.* Fe + Mg; (b) Si *vs.* K + Na + Ca; (c) K *vs.* Na; (d) Na/Na + K *vs.* Si/Al. Black circles and solid lines indicate the theoretical muscovite position and corresponding exchange vectors, respectively.

Table 2. Electron microprobe analyses (wt.%) for dioctahedral micas.

	SiO$_2$	Al$_2$O$_3$	MgO	FeO	TiO$_2$	K$_2$O	CaO	Na$_2$O	Total
LO-A-14 1 G1	50.20	33.16	1.08	3.27	0.15	8.79	0.05	0.99	97.85
LO-A-14 1 G3	47.59	32.10	1.23	3.54	0.17	8.68	0.02	0.74	94.22
LO-A-14 1 G8	52.93	30.14	0.86	3.01	0.22	7.92	0.02	1.03	96.30
LO-A-14 1 G10	47.89	32.13	1.27	3.36	0.12	8.66	0.08	0.99	94.67
LO-A-14 1 G12	48.65	33.45	1.18	3.67	0.24	8.50	0.12	1.00	97.01
LO-A-14 1 G14	48.45	33.24	0.83	2.92	0.26	7.85	0.10	1.85	95.67
LO-A-14 2 G11	46.61	33.21	1.03	3.48	0.17	8.41	0.03	1.04	94.11
LO-A-14 2 G15	47.22	35.63	0.76	2.41	0.14	6.09	0.09	2.52	94.96
LO-A-14 1 P2	52.67	33.31	0.89	3.15	0.56	7.12	0.10	2.11	100.04
LO-A-14 1 P15	46.02	35.63	0.51	2.13	0.95	4.38	0.13	3.55	93.40
LO-A-14 2 P5	46.03	36.36	0.41	1.86	0.31	3.10	0.14	5.04	93.30
LO-A-14 2 P9	45.81	36.25	0.47	2.35	0.15	5.65	0.11	3.45	94.34
LO-A-14 2 P12	45.84	34.81	0.52	2.78	0.82	5.85	0.13	3.06	93.94

the former from a fluid. Given the stability field of kaolinite, its growth was a low-temperature process (<200°C); however, it is difficult to establish from the available data whether such a process is related to the final step of the hydrothermal activity in the fault or whether it is the result of meteoric infiltration.

The role of clay minerals in the mechanical behaviour of the fault

Niemeijer & Vissers (2014) studied the frictional properties of the AMF rocks that ruptured during the 2011 earthquake, which included fault gouges and elongated lenses of phyllites from the protolith embedded in a cataclastic matrix. They identified greater frictional strength (μ) in the protolith-derived lenses (μ from 0.50 to 0.70 at room temperature and from 0.70 to 0.80 at elevated temperatures) than the gouge-derived samples (μ from 0.35 to 0.60 at room temperature and from 0.40 to 0.50 at elevated temperatures). The lower friction coefficients are consistent with the larger amounts of weak phyllosilicates identified in the gouges, which, in addition to contributing to fault weakness, also impact the mechanical stability of the fault under shear. The mechanical stability is also known as the velocity or rate dependence, where the friction rate parameter (a-b) describes the stability of the sliding surface. A positive value of a-b indicates velocity strengthening leading to fault creep, while negative values of a-b correspond to velocity weakening that may result in earthquake nucleation (Scholz, 1998). Gouges from the AMF show velocity-strengthening properties that migrate to a velocity-neutral value under simulated shallower conditions (Niemeijer & Vissers, 2014). However, the protolith-derived lenses show velocity-weakening properties, which suggests that earthquakes in the AFM are nucleated in these protolith-derived lenses. The occurrence of phyllosilicates or other weak minerals in a fault zone may promote distributed deformation and provide an explanation for fault weakness (Faulkner *et al.*, 2003, 2010; Collettini *et al.*, 2009).

Fragile behaviour of stronger minerals with high friction values and velocity-weakening behaviour such as quartz (0.6 < μ < 0.7;

Table 3. Structural formulae for dioctahedral micas normalized to $O_{10}(OH)_2$ on the basis of SEM/EDX and EPMA/WDX data.

	Si	Al^{IV}	Al^{VI}	Fe	Mg	Ti	$\sum$oct.	K	Ca	Na	$\sum$inter.
Micas from foliated bands											
EPMA											
LO-A-14 1 G1	3.22	0.78	1.74	0.18	0.10	0.01	2.02	0.72	0.00	0.12	0.85
LO-A-14 1 G3	3.18	0.82	1.72	0.20	0.12	0.01	2.05	0.74	0.00	0.10	0.84
LO-A-14 1 G8	3.42	0.58	1.71	0.16	0.08	0.01	1.97	0.65	0.00	0.13	0.78
LO-A-14 1 G10	3.19	0.81	1.71	0.19	0.13	0.01	2.03	0.74	0.01	0.13	0.87
LO-A-14 1 G12	3.16	0.84	1.72	0.20	0.11	0.01	2.05	0.70	0.01	0.13	0.84
LO-A-14 1 G14	3.18	0.82	1.75	0.16	0.08	0.01	2.01	0.66	0.01	0.24	0.90
LO-A-14 2 G11	3.12	0.88	1.75	0.20	0.10	0.01	2.05	0.72	0.00	0.13	0.86
LO-A-14 2 G15	3.09	0.91	1.84	0.13	0.07	0.01	2.06	0.51	0.01	0.32	0.84
SEM											
LO-A-4 3 2	3.28	0.72	1.75	0.10	0.20	0.00	2.05	0.79	0.00	0.08	0.88
LO-A-5 1 4	3.06	0.94	1.91	0.09	0.06	0.00	2.06	0.73	0.00	0.20	0.93
LO-A-5 3 6	3.02	0.98	1.79	0.07	0.04	0.11	2.01	0.70	0.02	0.21	0.93
LO-A-5 3 7	3.04	0.96	1.89	0.08	0.04	0.03	2.04	0.78	0.00	0.14	0.92
LO-A-4 4 2	3.16	0.84	1.85	0.07	0.13	0.02	2.07	0.51	0.00	0.31	0.82
LO-C-3 1 5	3.07	0.93	1.96	0.04	0.06	0.00	2.05	0.71	0.00	0.16	0.87
Micas from thin, ultrafine-grained bands											
EPMA											
LO-A-14 1 P2	3.28	0.72	1.72	0.16	0.08	0.03	2.00	0.57	0.01	0.25	0.83
LO-A-14 1 P15	3.05	0.95	1.83	0.12	0.05	0.05	2.05	0.37	0.01	0.46	0.84
LO-A-14 2 P5	3.04	0.96	1.87	0.10	0.04	0.02	2.03	0.26	0.01	0.64	0.92
LO-A-14 2 P9	3.03	0.97	1.85	0.13	0.05	0.01	2.04	0.48	0.01	0.44	0.93
LO-A-14 2 P12	3.05	0.95	1.78	0.15	0.05	0.04	2.03	0.50	0.01	0.39	0.90
SEM											
LO-A-4 3 3	3.24	0.76	1.59	0.19	0.27	0.03	2.08	0.84	0.00	0.10	0.94
LO-A-4 5 5	3.18	0.82	1.70	0.19	0.15	0.02	2.07	0.84	0.00	0.10	0.94
LO-A-4 6 2	3.17	0.83	1.76	0.17	0.13	0.03	2.08	0.81	0.00	0.06	0.87
LO-A-4 6 3	3.16	0.84	1.78	0.17	0.11	0.00	2.07	0.81	0.00	0.12	0.93
LO-A-4 6 5	3.11	0.89	1.84	0.12	0.10	0.02	2.07	0.77	0.00	0.09	0.87
LO-C-3 1 1	3.10	0.90	1.80	0.12	0.13	0.02	2.07	0.82	0.00	0.09	0.90
LO-C-3 1 6	3.05	0.95	1.88	0.08	0.06	0.02	2.04	0.73	0.00	0.24	0.97
LO-C-3 2 6	3.10	0.90	1.82	0.09	0.15	0.02	2.08	0.76	0.00	0.12	0.88
LO-A-4 5 2	3.01	0.99	2.01	0.03	0.00	0.00	2.04	0.19	0.00	0.71	0.90
LO-A-4 5 3	2.96	1.04	1.99	0.05	0.00	0.00	2.04	0.26	0.02	0.67	0.95
LO-A-4 5 4	3.08	0.92	1.97	0.04	0.00	0.00	2.01	0.20	0.03	0.68	0.91

inter. = interlaminar cations; oct. = octahedral.

Table 4. Structural formulae for chlorites and kaolinites normalized to $O_{10}(OH)_8$ on the basis of SEM/EDX data.

	Si	Al^{IV}	Al^{VI}	Fe	Mg	Mn	Ti	$\sum$oct.
Chlorites								
LO-A-4 2 1	2.54	1.46	1.43	2.68	1.84	0.00	0.00	5.95
LO-A-4 3 4	2.72	1.28	1.51	2.65	1.69	0.04	0.00	5.89
LO-A-4 4 1	2.79	1.21	1.56	2.56	1.60	0.00	0.00	5.73
LO-A-4 6 1	2.55	1.45	1.58	2.47	1.89	0.00	0.00	5.94
Kaolinites								
LO-A-5 3 1	3.96	0.04	4.01	0.00	0.00	0.00	0.00	4.01
LO-A-5 3 5	4.04	0.00	3.94	0.00	0.00	0.00	0.00	3.94
LO-A-5 3 8	3.94	0.06	4.02	0.00	0.00	0.00	0.00	4.02

oct. = octahedral.

Byerlee, 1978; Dieterich & Kilgore, 1994) may lead to cataclastic textures that increase rock permeability and create permeable paths. Fluid–rock interaction within the paths produces leaching of the host rocks and favours the crystallization of new minerals: submicroscopically, paragonite and phengite intergrowths located in the thin, ultrafine-grained bands and the rounded to lens-shaped micropods of kaolinite. In addition to the mineral changes, the interaction of low-temperature fluids and the fault rocks modifies the microstructural features of the gouges and might, as a consequence, alter the stability of the fault plane.

In particular, the authigenesis of expandable clay minerals in fault gouges may contribute to friction coefficients as low as 0.05 under wet conditions, as well as to velocity-strengthening behaviours (Lockner *et al.*, 2011). For this reason, the expandable minerals have often been related to fault creep and mechanical stability, as in the case of the central segment of the San Andreas Fault (Lockner *et al.*, 2011). Nevertheless, the AFM shows no evidence of authigenesis of expandable minerals in its fault gouges. On the contrary, all authigenic minerals are non-expandable. The frictional strength of kaolinite under wet conditions is high when compared with that of the expandable clay minerals: $\mu = 0.51$ (Moore & Lockner, 2004), $\mu = 0.53$ (Morrow *et al.*, 2000), $\mu = 0.29$ (Behnsen & Faulkner, 2012) and $\mu = 0.23$ (Brantut *et al.*, 2008).

As suggested by frictional data (Niemeijer & Vissers, 2014), earthquake nucleation in the AMF is concentrated in lenses of phyllitic basement rocks; immediately afterwards, rupture propagation takes place through the fault rocks. The absence of smectite within the fault gouges (only small amounts of smectite were identified in two of the studied samples) and the presence of kaolinite, quartz and micas may explain the observed velocity-neutral behaviour of this gouge and earthquake propagation towards the surface (Niemeijer & Vissers, 2014) instead of the velocity-strengthening behaviour characteristic of weak phyllosilicates that is expected to represent a barrier to rupture propagation.
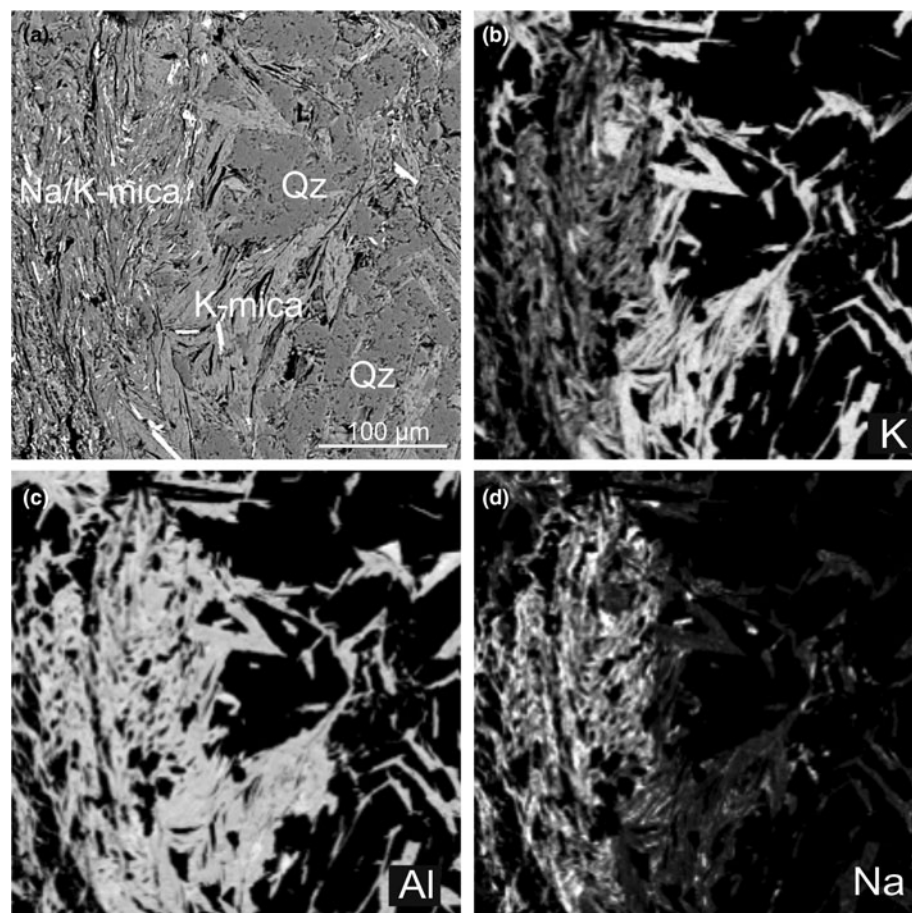
Fig. 10. BSE image (a) and K, Al and Na X-ray maps (b, c and d, respectively) of one of the selected zones analysed by EPMA and processed with *ImageJ*, where well-crystallized muscovites (right) and a fine-grained phyllosilicate band mainly composed of Na/K-micas (left) are observed.
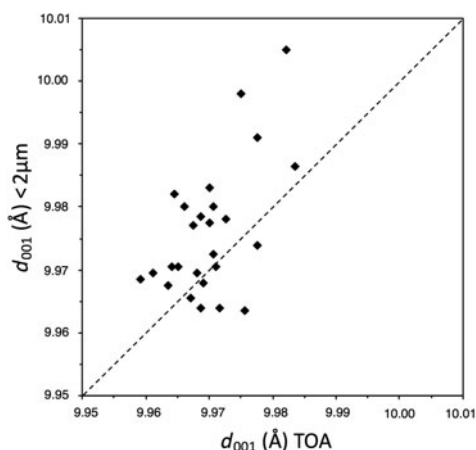

Fig. 11. Comparison between the mica d_{001} spacings of the <2 μm and whole fractions of the studied samples, calculated from the position of the (00,10) K-dioctahedral mica peak. TOA = total oriented aggregates.

Author ORCIDs. 🆔 Isabel Abad, 0000-0002-6354-0173

References

Abad I., Jiménez-Millán J., Schleicher A.M. & van der Pluijm B. (2017) Mineral characterization, clay quantification and Ar–Ar dating of faulted schists in the Carboneras and Palomares Faults (Betic Cordillera, SE Spain). *European Journal of Mineralogy*, **29**, 18–34.

Abad I., Nieto F., Peacor D.R. & Velilla N. (2003) Prograde and retrograde diagenetic and metamorphic evolution in metapelitic rocks of Sierra Espuña (Spain). *Clay Minerals*, **38**, 1–23.

Alfaro P., Delgado J., Sanz de Galdeano C., Galindo-Zaldívar J., García-Tortosa F.J., López-Garrido A.C., López-Casado C., Marín C., Gil A. & Borque M.J. (2008) The Baza Fault: a major active extensional fault in the Central Betic Cordillera (south Spain). *International Journal of Earth Sciences*, **97**, 1353–1365.

Alfaro P., Delgado J., García-Tortosa F.J., Lenti L., López A., López-Casado C. & Martino S. (2012) Widespread landslides induced by the Mw 5.1 earthquake of 11 May 2011 in Lorca, SE Spain. *Engineering Geology*, **137–138**, 40–52.

Arostegui J., Irabien M.J., Nieto F., Sangüesa J. & Zuluaga M.C. (2001) Microtextures and the origin of muscovite-kaolinite intergrowths in sandstones of the Utrillas Formation, Basque Cantabrian Basin, Spain. *Clays and Clay Minerals*, **49**, 529–539.

Azañón J.M. & Crespo-Blanc A. (2000) Exhumation during a continental collision inferred from the tectonometamorphic evolution of the Alpujárride

Complex in the central Betics (Alborán Domain, SE Spain). *Tectonics*, **19**, 549–565.

Behnsen J. & Faulkner D. (2012) The effect of mineralogy and effective normal stress on frictional strength of sheet silicates. *Journal of Structural Geology*, **42**, 49–61.

Bell J.W., Amelung F. & King G.C.P. (1997) Preliminary Late Quaternary slip history of the Carboneras fault, southeastern Spain. *Journal of Geodynamics*, **24**, 51–66.

Booth-Rea G., Azañón J.M., Azor A. & García-Dueñas V. (2004) Influence of strike-slip fault segmentation on drainage evolution and topography. A case study: the Palomares fault zone (southeastern Betics, Spain). *Journal of Structural Geology*, **26**, 1615–1632.

Bourdelle F. & Cathelineau M. (2015) Low-temperature chlorite geothermometry: a graphical representation based on a T-R^{2+} diagram. *European Journal of Mineralogy*, **27**, 617–626.

Brantut N., Schubnel A., Rouzaud J.N., Brunet F. & Shimamoto T. (2008) High-velocity frictional properties of a clay-bearing fault gouge and implications for earthquake mechanics. *Journal of Geophysical Research*, **113**, B10401.

Byerlee J. (1978) Friction of rocks. *Pure and Applied Geophysics*, **116**, 615–626.

Coggon R. & Holland J.B. (2002) Mixing properties of phengitic micas and revised garnet-phengite thermobarometers. *Journal of Metamorphic Geology*, **20**, 683–696.

Collettini C., Niemeijer A., Viti C. & Marone C. (2009) Fault zone fabric and fault weakness. *Nature*, **462**, 907–910.

Dieterich J.H. & Kilgore B.D. (1994) Direct observation of frictional contacts: new insights for state-dependent properties. *Pure and Applied Geophysics*, **143**, 283–302.

Duggen S., Hoernle K. & van der Bogaard H. (2004) Magmatic evolution of the Alboran region: the role of subduction in forming the western Mediterranean and causing the Messinian Salinity Crisis. *Earth and Planetary Science Letters*, **218**, 91–108.

Evans J.P. & Chester F.M. (1995) Fluid–rock interaction in faults of the San Andreas system; inferences from San Gabriel Fault rock geochemistry and microstructures. *Journal of Geophysical Research*, **100**, 13007–13020.

Faulkner D.R., Jackson C.A.L., Lunn R.J., Schlische R.W., Shipton Z.K., Wibberley C.A.J. & Withjack M.O. (2010) A review of recent developments concerning the structure, mechanics and fluid flow properties of fault zones. *Journal of Structural Geology*, **32**, 1557–1575.

Faulkner D.R., Lewis A.C. & Rutter E.H. (2003) On the internal structure and mechanics of large strike-slip fault zones: field observations from the Carboneras fault, southeastern Spain. *Tectonophysics*, **367**, 235–251.

Ferrater M., Booth-Rea G., Pérez-Peña J.V., Azañón J.M., Giaconia F., Masana E. (2015) From extension to transpression: Quaternary reorganization of an extensional-related drainage network by the Alhama de Murcia strike-slip fault (eastern Betics). *Tectonophysics*, **663**, 33–47.

Frey M. (1969) A mixed-layer paragonite/phengite of low-grade metamorphic origin. *Contributions to Mineralogy and Petrology*, **24**, 63–65.

Frey M. (1978) Progressive low-grade metamorphism of a black shale formation, Central Swiss Alps, with special reference to pyrophyllite and margarite bearing assemblages. *Journal of Petrology*, **19**, 95–135.

Gracia E., Pallas R., Soto J.I., *et al.* (2006) Active faulting offshore SE Spain (Alboran Sea): implications for earthquake hazard assessment in the Southern Iberian Margin. *Earth and Planetary Science Letters*, **241**, 734–749.

Guidotti C.V., Mazzoli C., Sassi F.P. & Blencoe J.G. (1992) Compositional controls on the cell dimensions of $2M_1$ muscovite and paragonite. *European Journal of Mineralogy*, **4**, 283–297.

Guidotti C.V., Sassi F.P., Blencoe J.G., & Selverstone J. (1994) The paragonite-muscovite solvus: I. P-T-X limits derived from the Na-K compositions of natural, quasi-binary paragonite-muscovite pairs. *Geochimica et Cosmochimica Acta*, **58**, 2269–2275.

IGN (2001) *Instituto Geográfico Nacional, Catálogo Sísmico Nacional hasta el 1900*. IGN, Madrid, Spain.

Imber J., Holdsworth R.E., Butler C.A. & Strachan R.A. (2001) A reappraisal of the Sibson–Scholz fault zone model: the nature of the frictional to viscous ('brittle–ductile') transition along a long-lived, crustal-scale fault, Outer Hebrides, Scotland. *Tectonics*, **20**, 601–624.

Jiang W.T. & Peacor D.R. (1993) Formation and modification of metastable intermediate sodium potassium mica, paragonite, and muscovite in hydrothermally altered metabasites from north Wales. *American Mineralogist*, **78**, 782–793.

Jiménez-Millán J., Abad I., Hernández-Puentes P. & Jiménez-Espinosa R. (2015) Influence of phyllosilicates and fluid–rock interaction on the deformation style and mechanical behaviour of quartz-rich rocks in the Carboneras and Palomares fault areas (SE Spain). *Clay Minerals*, **50**, 619–638.

Livi K.J.T., Christidis G.E., Árkai P. & Veblen D.R. (2008) White mica domain formation: a model for paragonite, margarite, and muscovite formation during prograde metamorphism. *American Mineralogist*, **93**, 520–527.

Lockner D.A., Morrow C., Moore D. & Hickman S. (2011) Low strength of deep San Andreas Fault gouge from SAFOD core. *Nature*, **472**, 82–85.

López-Comino J.A., Mancilla F., Morales J. & Stich D. (2012) Rupture directivity of the 2011, Mw 5.2 Lorca earthquake (Spain). *Geophysical Research Letters*, **39**, L03301.

Masana E., Martínez-Díaz J.J., Hernández-Enrile J.L. & Santanach P. (2004) The Alhama de Murcia Fault (SE Spain), a seismogenic fault in a diffuse plate boundary: seismotectonic implications for the Ibero-Magrebian region. *Journal of Geophysical Research*, **109**, B01301.

Martínez-Díaz J.J., Béjar-Pizarro M., Álvarez-Gómez J.A., Mancilla F.L., Stich D., Herrera G. & Morales J. (2012a) Tectonic and seismic implications of an intersegment rupture. The damaging May 11th 2011 Mw 5.2 Lorca, Spain, earthquake. *Tectonophysics*, **546–547**, 28–37.

Martínez-Díaz J.J., Masana E. & Ortuño M. (2012b) Active tectonics of the Alhama de Murcia Fault, Betic Cordillera, Spain. *Journal of Iberian Geology*, **38**, 269–286.

Meijninger B.M.L. & Vissers R.L.M. (2006) Miocene extensional basin development in the Betic Cordillera, SE Spain revealed through analysis of the Alhama de Murcia and Crevillente faults. *Basin Research*, **18**, 547–571.

Montenat C. & Ott D'Estevou P. (1995) Late Neogene basins evolving in the Eastern Betic transcurrent fault zone: an illustrated review. Pp. 372–386 in: *Tertiary Basins of Spain* (P.F. Friend & C.J. Dabrio, editors). Cambridge University Press, Cambridge, UK.

Moore D. & Lockner D. (2004) Crystallographic controls on the frictional behavior of dry and water-saturated sheet structure minerals. *Journal of Geophysical Research*, **109**, B03401.

Morrow C., Moore D. & Lockner D. (2000) The effect of mineral bond strength and adsorbed water on fault gouge frictional strength. *Geophysical Research Letters*, **27**, 815–818.

Niemeijer A.R. & Vissers R.L.M. (2014) Earthquake rupture propagation inferred from the spatial distribution of fault rock frictional properties. *Earth and Planetary Science Letters*, **396**, 154–164.

Nieto F., Velilla N., Peacor D.R. & Ortega-Huertas M. (1994) Regional retrograde alteration of sub-greenschist facies chlorite to smectite. *Contributions to Mineralogy and Petrology*, **115**, 243–252.

Parra T., Vidal O. & Agard P. (2002) A thermodynamic model for Fe–Mg dioctahedral K white micas using data from phase-equilibrium experiments and natural pelitic assemblages. *Contributions to Mineralogy and Petrology*, **143**, 706–732.

Pouchou J.L. & Pichoir F. (1985) 'PAP' (f) (r) (t) procedure for improved quantitative microanalysis. Pp. 104–106 in: *Microbeam Analysis* (J.T. Armstrong, editor). San Francisco Press, San Francisco, CA, USA.

Rutter E.H., Faulkner D.R. & Burgess R. (2012) Structure and geological history of the Carboneras Fault Zone, SE Spain: part of a stretching transform fault system. *Journal of Structural Geology*, **42**, 227–245.

Sanz de Galdeano C. (1990) Geologic evolution of the Betic Cordilleras in the western Mediterranean, Miocene to present. *Tectonophysics*, **172**, 107–119.

Schleicher A.M., Hofmann H. & van der Pluijm B.A. (2013) Constraining clay hydration state and its role in active fault systems. *Geochemistry, Geophysics, Geosystems*, **14**, 1039–1052.

Schleicher A.M., van der Pluijm B.A. & Warr L.N. (2010) Nanocoatings of clay and creep of the San Andreas Fault at Parkfield, California. *Geology*, **38**, 667–670.

Scholz C.H. (1998) Earthquakes and friction laws. *Nature*, **391**, 37–42.

Shau J.H., Feather M.E., Essene E.J. & Peacor D.R. (1991) Genesis and solvus relations of submicroscopically intergrown paragonite and phengite in a blueschist from northern California. *Contributions to Mineralogy and Petrology*, **106**, 367–378.

Sibson R.H. (1986) Earthquakes and rock deformation in crustal fault zones. *Annual Review of Earth and Planetary Sciences*, **14**, 149–175.

Solum J., van der Pluijm B., Peacor D. & Warr L. (2003) Influence of phyllosilicate mineral assemblages, fabrics, and fluids on the behavior of the Punchbowl fault, southern California. *Journal of Geophysical Research*, **108**, 2233.

Torgersen E. & Viola G. (2014) Structural and temporal evolution of a reactivated brittle-ductile fault – part I: fault architecture, strain localization mechanisms and deformation history. *Earth and Planetary Science Letters*, **407**, 205–220.

Vidal O., Lanari P., Munoz M., Bourdelle F. & de Andrade V. (2016) Deciphering temperature, pressure and oxygen-activity conditions of chlorite formation. *Clay Minerals*, **51**, 615–633.

Vrolijk P. & van der Pluijm B.A. (1999) Clay gouge. *Journal of Structural Geology*, **21**, 1039–1048.

Wang C.Y. (1984) On the constitution of the San Andreas Fault zone in Central California. *Journal of Geophysical Research*, **89**, 5858–5866.

Whitney D.L. & Evans B.W. (2010) Abbreviations for names of rock-forming minerals. *American Mineralogist*, **95**, 185–187.